# CFD-DEM simulations of a fluidized bed crystallizer

Kristin Kerst [a], Christoph Roloff [a], Luís G. Medeiros de Souza [a], Antje Bartz [c], Andreas Seidel-Morgenstern [b,c], Dominique Thévenin [a], Gábor Janiga [a,*]

[a] Institute of Fluid Dynamics and Thermodynamics, University of Magdeburg "Otto von Guericke", Magdeburg, Germany
[b] Institute of Process Engineering, University of Magdeburg "Otto von Guericke", Magdeburg, Germany
[c] Max Planck Institute for Dynamics of Complex Technical Systems (MPI), Magdeburg, Germany

## HIGHLIGHTS

- Examination of the complex two-phase flow in a fluidized bed crystallizer.
- CFD-DEM simulation of the crystallizer with non-growing crystals.
- Validation of the CFD-DEM simulation model via Shadowgraphy with a particle tracking approach.
- Identification of regions with unfavorable hydrodynamic features, thus negatively impacting process outcome.
- Determination of crystal position and relative crystal velocities within the crystallizer.

## ARTICLE INFO

## ABSTRACT

In the present study, important features of the two-phase flow in a fluidized bed crystallizer are examined by numerical computations and companion experiments. The simulations are carried out using a coupled CFD-DEM approach (CFD: Computational Fluid Dynamics; DEM: Discrete Element Method). After validating an open-source CFD-DEM software tool for this purpose, regions within the crystallizer with unfavorable hydrodynamic features and thus a negatively impacted process outcome have been identified. This was first accomplished by single-phase CFD simulations. Then, the validated CFD-DEM model delivers valuable information that is difficult or even impossible to measure experimentally with sufficient accuracy, such as the velocity and position of fluidized crystals within the crystallizer.

Since the simulations are computationally challenging, a compromise between simulated process time and number of simulated particles must be found. Hence, the CFD-DEM simulations are not utilized to simulate the whole crystallization process, but to examine a short time-window in detail. Corresponding findings confirm proper fluidization of the crystals support the model reduction carried out in a parallel project.

© 2017 The Authors. Published by Elsevier Ltd. This is an open access article under the CC BY-NC-ND license (http://creativecommons.org/licenses/by-nc-nd/4.0/).

## 1. Introduction

Crystallization is an important process in the chemical, pharmaceutical, and food industry and is the subject of many current research projects, e.g., (Reinhold and Briesen, 2015; Ochsenbein et al., 2015; Fang et al., 2015). In solid/liquid crystallizers, crystal growth is greatly influenced by the hydrodynamics (Ashraf Ali et al., 2013; Ashraf Ali et al., 2015). In comparison with solid–gas fluidized beds (Fries et al., 2013; Chen et al., 2015), studies pertaining to solid–liquid fluidization are relatively scarce in the scientific literature (Ashraf Ali et al., 2015; Qiu and Wu, 2014). A fluidized bed crystallizer is examined in the present study, with the ultimate objective of optimizing set-up and process conditions.

The process under investigation aims to realize the synthesis of a desired enantiomer as well as the separation of racemic mixtures by selective crystallization (Binev, 2015; Binev et al., 2016). Enantiomers are chemical molecules that spatially behave like mirror images of each other. They have identical physicochemical properties, but differ in their behavior in a chiral environment (e.g., in living organisms). As such, the use of pure enantiomers plays a particularly important role in life-science industries. Under certain conditions, crystallization can be used for enantiomer extraction. It is particularly advantageous that crystallization is both highly selective, thus leading to high purities, while simultaneously allowing a targeted particle design.

* Corresponding author.
  E-mail address: janiga@ovgu.de (G. Janiga).

**Nomenclature**

| | | | | |
|---|---|---|---|---|
| $\alpha$ | volume fraction (–) | | $v$ | velocity (m/s) |
| $c$ | damping constant (–) | | $x$ | spatial overlapping (–) |
| $d$ | diameter (m) | | $z$ | vertical axis of the crystallizer or column (m) |
| $F$ | force (N) | | | |
| $h$ | height (m) | | *Subscripts* | |
| $k$ | stiffness (–) | | $b$ | body |
| $p$ | pressure (Pa) | | $f$ | fluid |
| $R$ | momentum exchange (N/m$^3$) | | $i, j$ | contact partners |
| $\rho$ | density (kg/m$^3$) | | $n$ | normal |
| $t$ | time (s) | | $p$ | particle |
| $\tau$ | stress tensor (Pa) | | $t$ | tangential |
| $N$ | number (–) | | $z$ | vertical coordinate of the crystallizer or column |
| $v$ | kinematic viscosity (m$^2$/s) | | | |

To produce fine chemicals, batch processes are typically used. However, in order to ensure constant product quality, but also to allow for larger production capacities (e.g., to produce aminoacids), continuous crystallization processes would be a very attractive alternative.

The development and optimization of a continuous crystallization process is currently the subject of intense research activities in our group, as described in particular in Qamar et al. (2013), Lorenz and Seidel-Morgenstern (2014), Fayzullin et al. (2014), Eicke et al. (2013). Fig. 1 shows the basic structure of the novel operating process.

Two identically-built crystallizers constitute the main part of the process. The two crystallizers are connected in parallel and a reaction runs synchronously in both crystallizers. This allows producing simultaneously two outlet streams; each contains just a single enantiomer. Although typically only one of the enantiomers is the target, the continuous production of the second one is also very attractive. The counter-enantiomer can be applied for other applications (e.g., as a building block for further chiral molecules) or it can be racemized and recycled. The crystallizers are continuously supplied with a saturated solution of a racemic solid via a feed tank. The inlet is located at the bottom of the crystallizer. To start the crystallization process, fixed amounts of enantiopure seed crystals are given initially in each of the two crystallizers. Thus, one crystallizer initially contains the desired enantiomer, while the other crystallizer contains the counter-enantiomer. The selective growth of the seed crystals reduces the supersaturation of the solution in both vessels. The solutions with the remaining enantiomer leave the crystallizer at the top and are returned via heated lines (in order to dissolve them) to the feed tank, before re-circulating. Meanwhile, particles of a specific size are drawn off as a suspension in the middle part of the crystallizer. To ensure that the process runs continuously, particles below a certain size are continuously transported out at the top of the crystallizer while particles of larger sizes, which sink to the bottom of the crystallizer, are transported into an ultrasonic bath where they are crushed. The crushed particles are transported back into the crystallizer and act as seeds. Significant advantages of the process are the recycling of both (1) the undesired enantiomer, and of (2) all crystals that are not in the target size area (too small or too large). Furthermore, the connection of the two vessels increases in both cases the growth rate of the target enantiomer and suppresses the tendency for unwanted nucleation of the counter-enantiomer.

Fig. 2 shows the setup operated at the Max Planck Institute for Dynamics of Complex Technical Systems (MPI), Magdeburg, Germany. The crystallizers are visible in the framed boxes. The feed
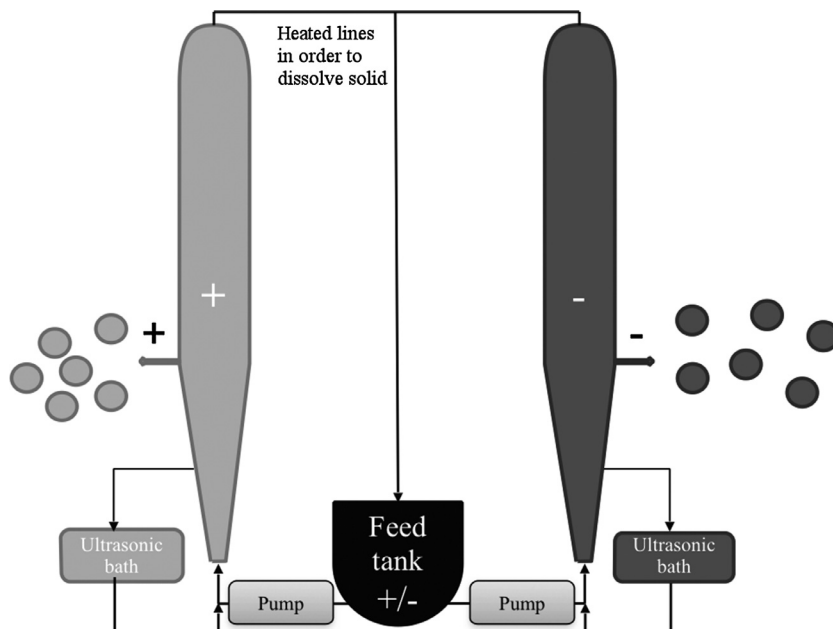


**Fig. 1.** Principle of the novel continuous crystallization process for the synthesis of a desired enantiomer.

tank is placed below. Though the crystallizer is already in operation, the results obtained could still be further optimized. One major problem is that the position of the crystals within the crystallizer as a function of their size cannot be predicted theoretically or measured experimentally, due to unknown hydrodynamics, poorly characterized fluidization behavior, opacity, and limited instrumentation. Considering that experimental measurements under real conditions are extremely difficult to carry out, accurate simulations are essential to supply valuable information and guide process improvement, opening the door for process optimization (Daróczy et al., 2014) based on coupling computational fluid dynamics (CFD) with discrete element method (DEM).

Such coupled CFD-DEM simulations constitute a relatively new, but promising, approach for the simulation of multiphase flows (Harris et al., 1996; Fries et al., 2011). CFD-DEM calculations belong to the so-called four-way coupling methods (Crowe, 2005), which means that

1. the fluid (continuous phase) influences the particles,
2. the particles have an influence on the fluid flow,
3. particle disturbance of the fluid locally affects the motion of other particles as well (an effect often called particle swarm), and
4. the particles can collide with one another as well as with the crystallizer walls.

The advantage of CFD-DEM simulations compared to simpler multiphase models, e.g., Discrete Phase Simulations (DPM), is that particle–particle interactions are directly taken into account, as well as the flow modifications due to swarm effects. In the fluidized bed crystallizer considered here, these interactions have a noticeable impact, as the suspension density is very high, explaining the need for CFD-DEM simulations (Ashraf Ali et al., 2013; Ashraf Ali et al., 2015) instead of, e.g., DPM. The average solid volume fraction in the simulations of the crystallizer with the lowest suspension densities is 0.00031; the maximum solid volume fraction is 0.01631. According to Sommerfeld et al. (2008), particle–particle-interactions have to be taken into account as soon as solid volume fraction is higher than 0.0004. This condition is clearly fulfilled here.



**Fig. 2.** Existing test apparatus installed at MPI Magdeburg.

This paper first provides a brief description of the employed CFD-DEM model, before discussing simulation models and measurement data in more detail. In order to validate the CFD-DEM simulations with companion validation experiments, tests with fluidized particles were performed in a specially designed test crystallizer using inert, spherical glass beads instead of crystals. In the rest of this paper the experiments in the original crystallizer are denoted by Setup 1, the experiments in the specially designed test crystallizer with glass beads are denoted by Setup 2. Then, areas with unfavorable hydrodynamic features were identified by CFD simulations, and solutions were proposed and implemented to solve these issues. The validated CFD-DEM simulations provide valuable information to foster process understanding, such as velocities (both absolute and relative) and positions of fluidized crystals. Since such simulations are computationally challenging, a compromise between simulated process time and number of simulated particles must be found. As a consequence, only a few seconds of the process can be simulated. In this small time frame, crystal growth is negligible. Hence, the CFD-DEM simulations are not used to simulate the whole crystallization process, but rather to examine selected issues controlling and impacting the process outcome, focussing on the details of the two-phase flow.

## 2. Computational model

In this section the computational details of the CFD-DEM simulation are briefly described. Further general details concerning CFD-DEM can be found, e.g., in Zhu et al. (2007), Zhu et al. (2008).

### 2.1. DEM

In DEM, the physical particles are usually mathematically approximated as spheres (Freireich et al., 2015). Other shapes may be in principle represented by interconnecting spherical particles, but at the expense of a considerably higher computational effort. To save computational time, for the current CFD-DEM simulations, all particles are assumed to be spherical. A separate project confirmed that the fluidization behavior remains nearly unchanged when taking non-spherical fluidized crystals into account, while the required computational time increases considerably.

A soft sphere contact model according to Cundall and Strack (1979) based on correlations of Hertz (1882) and Mindlin (1949) was applied. In contrast to the hard-sphere approach, the soft-sphere approach allows a virtual overlap of the particles (Müller and Tomas, 2014). The particle motion is based on the Lagrangian approach, which means that each particle trajectory is solved explicitly by tracking its movement. The corresponding momentum balances serve as the basis in computing the translational and angular accelerations of each particle. Summing up all forces acting on a particle, one obtains:

$$F_{total} = F_n + F_t + F_f + F_b, \tag{1}$$

where $F_n$ is the normal force, $F_t$ is the tangential contact force, $F_f$ is the force that the fluid exerts on the particles, and $F_b$ is the body force that encompasses gravity as well as possible electrostatic and magnetic forces. In the present simulations, $F_b$ only describes gravity.

The forces acting on two contact partners $i$ and $j$ consist of the elastic and inelastic (damping) components (Salikov et al., 2015).

The normal force $\vec{F}_n$ is associated with the repulsion between the particles and can be estimated by the spatial overlapping between the particles $\Delta x_p$ and the relative velocity at the contact point $\Delta v_n$:

$$\vec{F}_n^{(ij)} = \left( k_n^{(ij)} \Delta x_p^{(ij)} + c_n^{(ij)} \Delta v_n^{(ij)} \right) \vec{n}_{ij}. \tag{2}$$

The components $k_n^{(ij)}$ and $c_n^{(ij)}$ describe the stiffness and the damping constant.

The tangential force $\vec{F}_t$ depicts the elastic tangential deformation of the particle surfaces and the energy dissipation of the tangential contact:

$$\vec{F}_t^{(ij)} = \left( k_t^{(ij)} \Delta x_p^{(ij)} + c_t^{(ij)} \Delta v_t^{(ij)} \right) \vec{t}_{ij}. \tag{3}$$

The components of the contact forces are dependent on particle properties, such as the density, the particle radius, the Poisson number, rolling friction coefficient and the Young's modulus. The employed values are listed in Table 1. For the Young's modulus, a non-realistic value is used, which is a common practice in DEM simulations in order to save computational time (Blais et al., 2016).

## 2.2. CFD-DEM

To describe the movement of an incompressible fluid with particles, the conservation of mass (or continuity) equation and the conservation of momentum (or Navier–Stokes) equation are written as follows:

$$\frac{\partial(\rho_f \alpha_f)}{\partial t} + \nabla \cdot (\rho_f \alpha_f v_f) = 0 \tag{4}$$

$$\frac{\partial(\rho_f \alpha_f v_f)}{\partial t} + \nabla \cdot (\rho_f \alpha_f v_f v_f) = -\alpha_f \nabla p + R_{f,p} + \nabla \cdot (\alpha_f \tau_f), \tag{5}$$

where index $f$ denotes the fluid, $\alpha_f$ represents the volume fraction locally occupied by the fluid, $\rho_f$ its density, $t$ is time, $v_f$ is the fluid velocity, $p$ is pressure, $\tau_f$ is the stress tensor and $R_{f,p}$ is the momentum exchange between fluid and particles. The drag force describing the multi-particle–fluid interaction is computed using the drag model of Di Felice (1993), commonly employed to describe fluidization (Zhou et al., 2011).

In practice, when a very large number of particles is simulated (as in the present case), a so-called *non-resolved* approach is used (Goniva et al., 2012). In this case the particles are much smaller than the Eulerian grid used to compute the flow. Consequently,

individual particles are not resolved explicitly in the CFD simulation, but are taken into account on the fixed Eulerian grid of the CFD computation through the field of volume fraction $\alpha_f$ (for the fluid phase), or $1 - \alpha_f$ (for the solid phase). In the present CFD-DEM calculation, the void fraction model called "center" is used (Goniva and Kloss, 2016). The "center" void fraction model calculates the void fraction in a CFD cell accounting for the volume of the particles whose centers are inside the cell. This well-established model leads to the shortest computational times compared with other void fraction models, e.g. "divided", where satellite points are used to divide the particle's volume to the cells touched. In order to further reduce the required computational resources, the ratio between cell volume of the Eulerian grid and particle volume is about 1000 in the present study. This value is unusually large, highlighting the necessity for a proper grid-independence study and validation concerning fluidization velocities, as discussed in the following.

The material properties of the crystals (glass and asparagine monohydrate) have first to be measured or calibrated, before using them in the CFD-DEM simulation. The wall friction coefficient was determined using a Jenicke-shear cell. In order to determine the angle of repose (a required parameter in LIGGGHTS), the bulk material was filled in a cylinder (diameter $\approx$ 100 mm, volume $\approx$ 1.5 dm$^3$), which is then moved upwards with a defined velocity of 8 mm/s. The angle of repose was determined via image analysis. The rolling friction coefficient has to be obtained from calibration simulations (again, those with the moving cylinder), for which parameters are varied until the observed behavior of the bulk material is correctly reproduced in the simulation.

## 2.3. Computational setup

CFD-DEM simulations are computationally challenging, which limits either the number of simulated particles or the duration of the simulation. Using powerful parallel computers is absolutely necessary for CFD-DEM simulations involving many particles, since the computational effort rapidly becomes unacceptable for such simulations (Wu et al., 2014). The benefit of parallelization for the configuration of interest is depicted in Fig. 3. The given computational times (in hours) correspond to a real process time of only 1 s.

In the current work, the full-scale three-dimensional fluidized bed crystallizer is simulated, since its geometry controls the hydrodynamics and outcome of the continuous process. The CFD-DEM
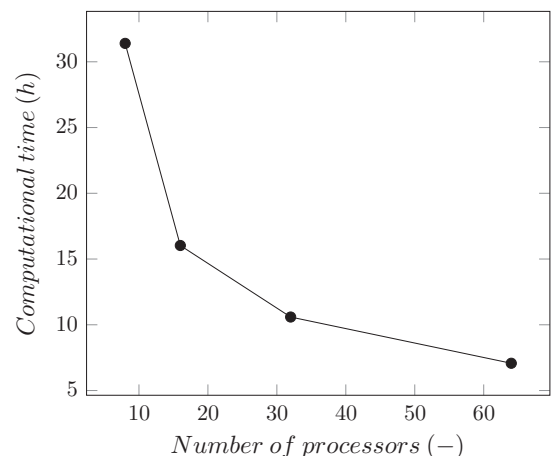
**Table 1**
CFD-DEM simulation parameters for the validation in Setup 2 (central column) and for the simulation of the real conditions in Setup 1 (right column).

| | Simulations for model validation | Simulations with asparagine mono-hydrate crystals |
|---|---|---|
| Vertical region of initial particle injection | 0.5–0.7 m | 0.5–0.7 m |
| Particle density | 2500 $\frac{kg}{m^3}$ (glass) | 1450 $\frac{kg}{m^3}$ (asparagine) |
| Number of particles | 100 000 | 200 000 |
| Total mass of particles | 0.248 g | 0.319 g |
| DEM timestep | 0.5 $\mu s$ | 0.5 $\mu s$ |
| Young's modulus | $10^7$ Pa | $10^7$ Pa |
| Poisson ratio | 0.3 | 0.235 |
| Rolling friction coefficient | 0.2 | 0.001 |
| Wall friction coefficient | 0.13 | 0.61 |
| Angle of repose | 31° | 19° |
| Kinematic viscosity (Verein deutscher Ingenieure (VDI-GVC), 1997) | $1.004 \times 10^{-6} \frac{m^2}{s}$ | $1.004 \times 10^{-6} \frac{m^2}{s}$ |
| Velocity at wall | no slip: 0 $\frac{m}{s}$ | no slip: 0 $\frac{m}{s}$ |
| Number of grid cells | 240640 | 191160 |
| CFD timestep | 100 $\mu s$ | 100 $\mu s$ |
| Coupling interval | 200 $\mu s$ | 200 $\mu s$ |
| Force models | Di Felice (1993) +buoyancy | Di Felice (1993) +buoyancy |
| Total physical simulation time | 60 s | 15 s |
| Total computing time | 302 h | 139 h |
| Processors used (Section 2.3) | 32 | 64 |



**Fig. 3.** Computational time over number of processors used for the considered crystallizer.

simulations take 200 000 particles into account. Though this value is very high, it must be kept in mind that one crystallizer typically contains 170 million crystals in reality.

Thus, two conclusions can be drawn. The good news is that parallelization can be used to noticeably speed-up the simulation process; using 64 instead of 8 processors can reduce the simulation time by a factor of almost 5. However, the bad news is that parallelization is not sufficient to simulate the entire process (several hours) using the real number of particles (about 170 million crystals): using the results of Fig. 3, such a simulation would still take years using hundreds of processors on a supercomputer. Fortunately, it is not necessary to solve the entire process in all of its complexity to acquire useful information from such simulations, as shown in the following. Simulating only a short time-frame of the process (neglecting crystal growth) with a reduced number of particles readily delivers essential information for process understanding and improvement.

To describe the entire process including growth, repeated full-scale 3D simulations of a short time-frame separated by a large timespan $\Delta t$ (of the order of 30 min) are currently being combined with homogeneous, 0D simulations in-between, accounting for crystal growth based on frozen hydrodynamics. The full-scale 3D simulations deliver crystal position, crystal size distribution (CSD), and crystal slip velocity compared to the surrounding flow; this information can readily be used to model crystal growth in the 0D simulations (Ashraf Ali et al., 2015), before re-starting a full-scale 3D simulation when growth has induced noticeable changes of the CSD. This model reduction approach will be described in a separate study.

The focus of the current work is on the exact determination of crystal velocities (both absolute and relative) and positions within the crystallizer as function of crystal size, at reduced suspension densities. An alternative model that accounts for high suspension densities and crystal growth but with highly simplified hydrodynamics is considered in a companion project (Mangold et al., 2014). Combining the results from both models shall ultimately allow process optimization.

All full-scale simulations have been carried out on an in-house Linux cluster using at least 32 processors (2100 Ghz/AMD Opteron quad-processor with high-speed Infiniband network connection).

### 2.3.1. CFD simulations

CFD simulations provide valuable information about the flow conditions found in the apparatus. Therefore, pure CFD simulations were carried out for the continuous liquid phase first, neglecting the particles. This corresponds to the start-up of the real crystallization process, before adding the seed crystals to the crystallizer. For all of the flow simulations discussed in this paper, the open-source software OpenFOAM 2.2.x (The OpenFOAM, 2016) was used.

Two similar configurations are considered. Setup 1 corresponds to the complete three-dimensional geometry of the fluidized bed crystallizer employed in reality. The utilized block-structure computational mesh is illustrated for Setup 1 in Fig. 4. The total crystallizer height is 1.18 m and the diameter of the central crystallizer at the product outlet nozzle is 0.03 m.

The second geometry, denoted Setup 2, is similar to Setup 1 but slightly simplified (no connecting tubes) and completely cylindrical, instead of conical. It was used to validate the computational models by comparison with experimental data, and will be described in more detail in Section 3.

The fluid (continuous) phase is water, hence incompressible. Additionally, the flow is always considered to be laminar, since the maximum diameter-based Reynolds number in both setups, found at the smallest cross-section near the inlet of Setup 1 (bottom part of Fig. 4), is 1710, and thus far below commonly accepted
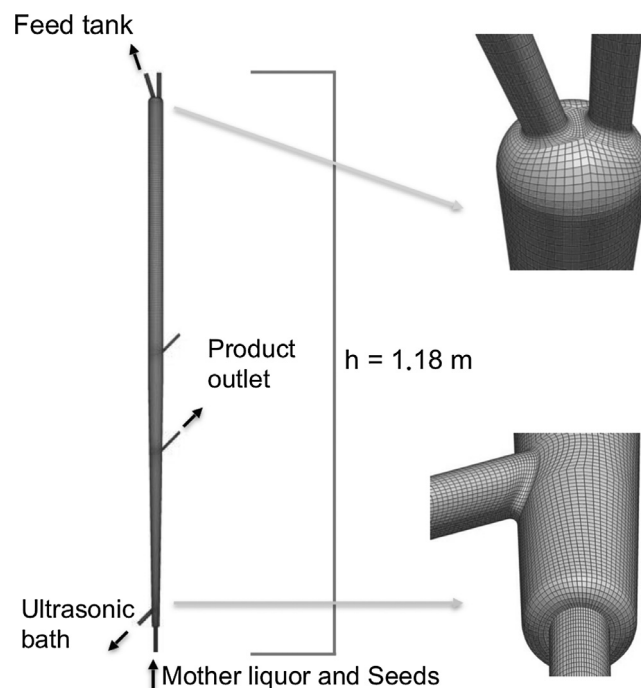


**Fig. 4.** Employed geometry and block-structure computational grid. Left: full view. Right: details.

values characterizing the onset of transition to turbulence in pipe flows; further above, the Reynolds number is obviously much lower, due to the increased crystallizer diameter and to the extraction of part of the liquid to the ultrasonic bath.

In order to check grid independency for CFD, a systematic simulation of Setup 2 with an injected volume flow rate of 25.1 L/h was performed on successively refined grids involving 30 080, 101 250, 240 640 and 470 000 finite-volume cells, respectively. Compared to the reference solution (that on the finest grid), the obtained volumetric flow rate with only 30 080 cells shows a relative error of 2.6% concerning the flow-rate obtained in the cross-section at a column height of 0.5 m (column mid-height), at the level where particles will later be injected in companion experiments. This difference is still too large for accurate simulations. On the other hand, the grid with 240 640 cells leads to a relative error below 0.2% compared to the reference, which is fully acceptable. A resolution with at least 240 640 cells has thus been retained for the later simulations. The obtained cell size was then kept identical when simulating the full-scale apparatus, Setup 1. Note that the number of grid cells needed for Setup 1 is slightly less than for Setup 2, due to the conical arrangement.

### 2.3.2. CFD-DEM simulations

In order to save computational time, each CFD-DEM simulation is systematically initialized with the pressure and velocity fields obtained from a previous CFD simulation at steady-state for the continuous (liquid) phase, without particles. The CFD-DEM simulations are performed using the open-source software CFDEMcoupling (Goniva and Kloss, 2016). The software CFDEMcoupling was developed by combining two well-known existing, open-source software (written in C++): OpenFOAM (for CFD) and LIGGGHTS (for DEM). The solution is obtained by combining the fluid (CFD) and particle (DEM) calculations using these two separate codes. The interaction is realized by exchanging relevant information with a predefined time step, as described in (Goniva et al., 2010). For the CFD simulation the transient solver *pisoFoam* of OpenFOAM is used. As its name states, this solver relies on the PISO algorithm

(Pressure Implicit with Splitting of Operator) for pressure–velocity coupling.

The real process in Setup 1 involves asparagine monohydrate crystals in the crystallizer. The cumulative crystal size distribution (CSD) function $Q_3$ of the asparagine crystals during process time when crystals are grown to the desired crystal size distribution was determined by optical measurement with a CAMSIZER XT (Retsch GmbH, Haan, Germany) and is depicted in Fig. 5. This CSD will be implemented in Setup 1, considering 200 000 crystals. For the validation experiments in Setup 2, 100 000 particles are injected in reality, and this number is retained in the CFD-DEM simulations. All further parameters for the CFD-DEM simulations of both setups are shown in Table 1 (left column for Setup 2, right column for Setup 1).

## 3. Validation of the CFD-DEM simulation model

Due to the complexity of the resulting simulation model, a proper validation of the developed approach is absolutely necessary. Here, this is performed with dedicated experiments in Setup 2. For this purpose, inert glass particles were injected into the flow. Obviously, such particles will not grow, but this is sufficient to review particle trajectories and verify that the numerical model is able to reproduce the correct fluidization behavior. The employed glass particles particle size distribution (PSD), $Q_3$, obtained by the CAMSIZER XT (Retsch GmbH, Haan, Germany) is depicted in Fig. 6. For the CFD-DEM simulation in this case, the same PSD has been discretized by 22 equidistributed classes. In the simulation all particles are initially injected at mid-height of the column using volume injection, which is similar to the experiments.

The identification of a suitable measurement technique to inspect the particle velocities proved to be a major challenge in the end. All available in-line measurement probes often used in real crystallizers (e.g., Endoscopy, Focused Beam Reflectance) were found to noticeably impact the hydrodynamics inside the crystallizer, and were thus rejected. As the walls are transparent (glass), using non-intrusive, image-based measurement techniques from outside would, in principle, be possible. Particularly, the Shadowgraphy technique, which is able to track suspended particles by recording their shadow images, seemed promising in this case. However, with the real crystallizer design in Setup 1, employing this method with sufficient quality proved impossible due to severe light refractions from the crystallizer jacket, since the crystallizer uses a thick double-jacket for temperature control. Light
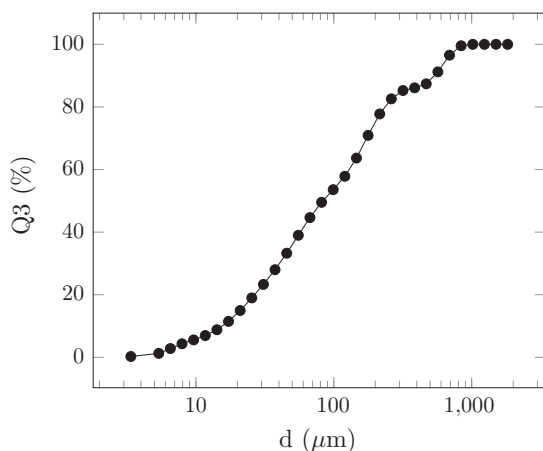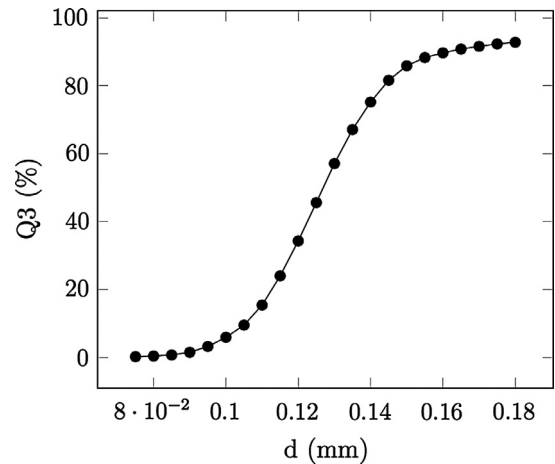
**Fig. 6.** Measured cumulative particle size distribution function $Q_3$ of the glass beads in Setup 2.

refraction taking place at four strongly curved interfaces (from outside to inside: air - glass - water - glass - water) leads to an unacceptable distortion of the light beams.

To solve this problem, a second column was built (see Setup 2 shown in Fig. 7, left), with dimensions slightly smaller but similar to the real crystallizer in Setup 1. It consists of a single-jacket column made of Makrolon material with an inner diameter of 26 mm and a height of 1050 mm. This cylindrical tube is embedded into a surrounding, transparent square-shaped duct with a side width of 100 mm. The space between the cylindrical column and the surrounding duct is filled with water. Hence, the change in refractive index is now limited to the small difference between water and the thin Makrolon wall, leading only to minor refraction, whereas the large difference between refraction index of air and Makrolon is no longer of practical relevance, since the camera acquires images perpendicular to the flat outer boundary of the square-shaped jacket. Overall, an excellent signal quality is obtained in this manner in Setup 2.

The Shadowgraphy measurement setup is depicted in Fig. 8. The column (1) is connected to a gear-pump (ISMATEC ISM405A) (5), which drives the flow in a controlled and constant manner from the lower (7) to the upper reservoir (8). The continuous flow rate is monitored by an ultrasonic flow meter (Sonotec, Halle, Germany; number 6). Homogeneous background illumination for particle tracking is provided by a Dedocool tungsten light head (Dedotec, Ashley Falls, USA; number 2) in combination with an optical diffusor plate (3). A camera (ImagerPro HS, LaVision, Göttingen, Germany; number 4) records the particle shadows in opposite direction to the light source at mid-height of the column.

Prior to the measurement runs, the camera images must be dewarped and scaled. To this end, a half-cylinder with a known printed dot pattern (Fig. 7, right) was manufactured, positioned inside the water-filled column and imaged. All measurements take place at a constant water flow rate of 25.1 L/h. A total mass of 2.5 mg of glass particles, which amounts to about 100 000 particles, is injected at mid-height of the column via a pipette. After injection, manual triggering of the camera system starts the measurement for a single run, which lasts 300 s in total, whereby the camera records double images every 5 s. This relatively long time delay between the acquisition of two image pairs is due to the slow velocities found in the apparatus and removes biased statistics that would result from multiple considerations of the same particles. The time delay between the double images in a pair was set to 5 ms, resulting in a frame rate of 200 Hz, which allows for reliable particle tracking. For post-processing and data analysis, the Particle Master Shadowgraphy software package by DaVis 8.2 (LaVision,
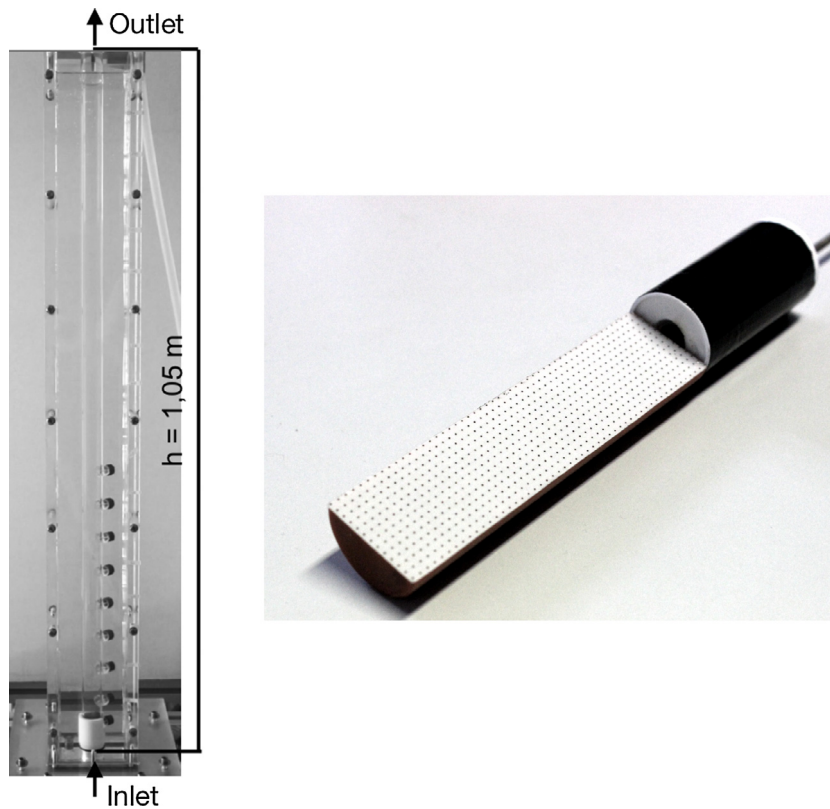
**Fig. 5.** Measured cumulative particle size distribution function $Q_3$ of the asparagine crystals in Setup 1.

**Fig. 7.** Left: Model crystallizer column for validation; right: target for camera calibration.
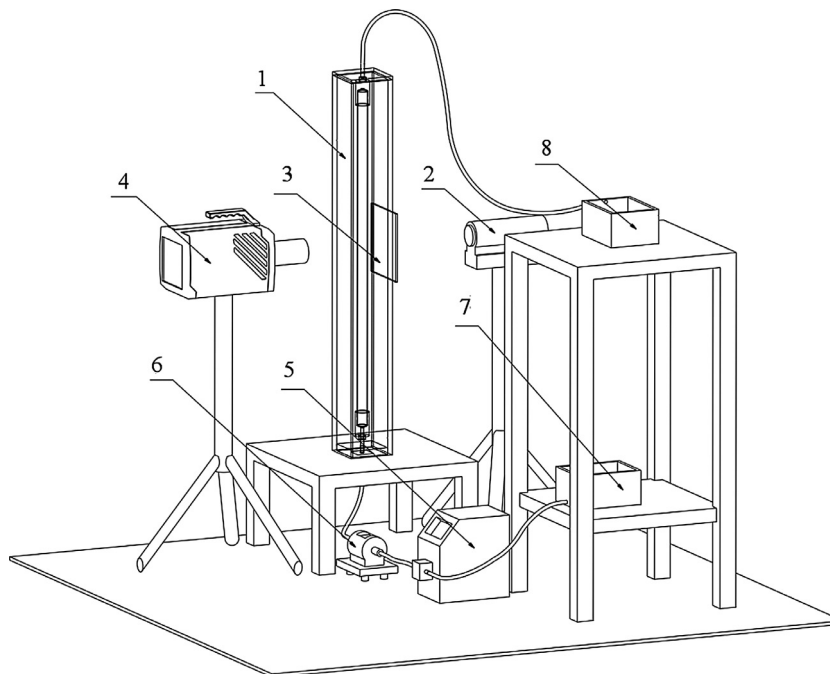


**Fig. 8.** Shadowgraphy setup for the validation experiment in Setup 2 with the column (1), tungsten light head (2) with an optical diffusor plate (3), camera (4), water cycle driven by a gear pump (5), flowmeter (6), and water reservoirs (7 and 8).

Göttingen, Germany) was used for particle identification, segmentation, sizing, and velocity estimation.

Glass particles below 100 μm often tend to agglomerate. In order to ensure consistency of the processing, all processed experimental images were checked manually. Indeed, a few particles have been found to agglomerate. These isolated agglomerates have not been included into the comparisons, since our observations indicate that these agglomerates already formed during the injection, and did not result from collisions in the crystallizer. Thus, adhesion models have not been activated in CFD-DEM-simulations.

All parameters retained for the CFD-DEM simulations of Setup 2 are shown in the central column of Table 1.

In Figs. 9 (experiment) and 10 (CFD-DEM simulation) the vertical velocity, $v_z$, of all fluidized particles that were observed at mid-height of the column ($z = 0.5$ m) over a total duration of 55 s are plotted as function of their radial position. The size of the employed markers is thereby proportional to the square diameter of the particles, so that it is easily possible to differentiate between small and large particles. These two figures can be used to examine the fluidization behavior of the particles within the column.

First, the decreasing rising velocity from left to right, from the column axis towards the outer wall of the column, can be observed, following, as expected, the parabolic profile of a laminar flow inside a cylindrical tube.

As expected, larger particles mostly feature lower velocities, while smaller particles tend to appear at the high-velocity side (top boundary) of the point cloud. Noticeable outliers appear only at the two earliest time points, where the influence of initial particle injection dominates particle motion.

Comparing both figures in detail, the rising velocity of the particles appears to be very close in CFD-DEM simulation and experiment. This agreement can be further quantified by means of Fig. 11, where the average particle velocities and the corresponding standard deviations are plotted over the same time interval as a function of the radial position (discretized in bins of 0.25 mm size). Considering that there are very few particles near the wall, this region is neglected in the analysis. Qualitatively, the trends are identical, especially regarding the vertical velocities in the center of the column, where the particles rise. Around a radial position of $\approx 10$ mm, some particles start changing direction (some rise, some sink), in the experiment like in the simulation. Quantitatively, numerical and experimental observations overlap when taking the standard deviation into account. Numerical diffusion might explain growing differences near the wall, since near-wall grid resolution has a high impact. Further simulations are currently ongoing on even finer grids to examine that point. They are, however, extremely time-consuming.

Considering the perfect qualitative agreement, the excellent identification of the transition between upward and downward movement of the particles, and the acceptable quantitative agree-ment concerning particle velocities, the developed approach can now be employed for the real process in Setup 1.

## 4. Results

### 4.1. Identifying hydrodynamic problems within the crystallizer

As a starting point, single-phase CFD simulations readily provide useful information in identifying hydrodynamic problems in the crystallizer, corresponding to the conditions found before introducing the crystal seeds. The total physical simulation time for this pure CFD simulation is 180 s, which corresponds to two bulk liquid flow-through times through the crystallizer. The flow-through time (or residence time) is computed as the crystallizer volume divided by the volumetric flow rate.

#### 4.1.1. Product outlet nozzles

The velocity magnitudes determined by CFD in the entire crystallizer in Setup 1 are shown in Fig. 12(a).

This figure shows the central vertical plane cutting the outlet nozzles at a physical time of 180 s (end of the simulation). As expected, due to the reduced diameters, the highest velocities are found at the crystallizer inlet and outlet, while the lowest velocities are found in the upper half part of the crystallizer, beginning at the level of the product outlet nozzles. It is visible in Fig. 12(b) that the product outlet nozzles locally lead to a flow distortion just downstream of the junction with the central draft tube; large-scale structures appear there and lead to unsteady flow features, before being dissipated and returning to a fully laminar flow state further upwards. This highly inhomogeneous flow is an undesired feature for the considered process.

In order to investigate this issue, experiments were performed in the full-scale crystallizer (Setup 1) with colored, monodisperse glass particles, allowing direct visualization of the pathlines. The glass particles are injected through an outlet nozzle with a syringe. Fig. 12(c) shows a close-up view of the outlet nozzle during such an experiment. Even when the product outlet nozzles are closed during the process, they still act as a sudden increase in flow cross-section at that level, leading to a reduction of flow velocities and
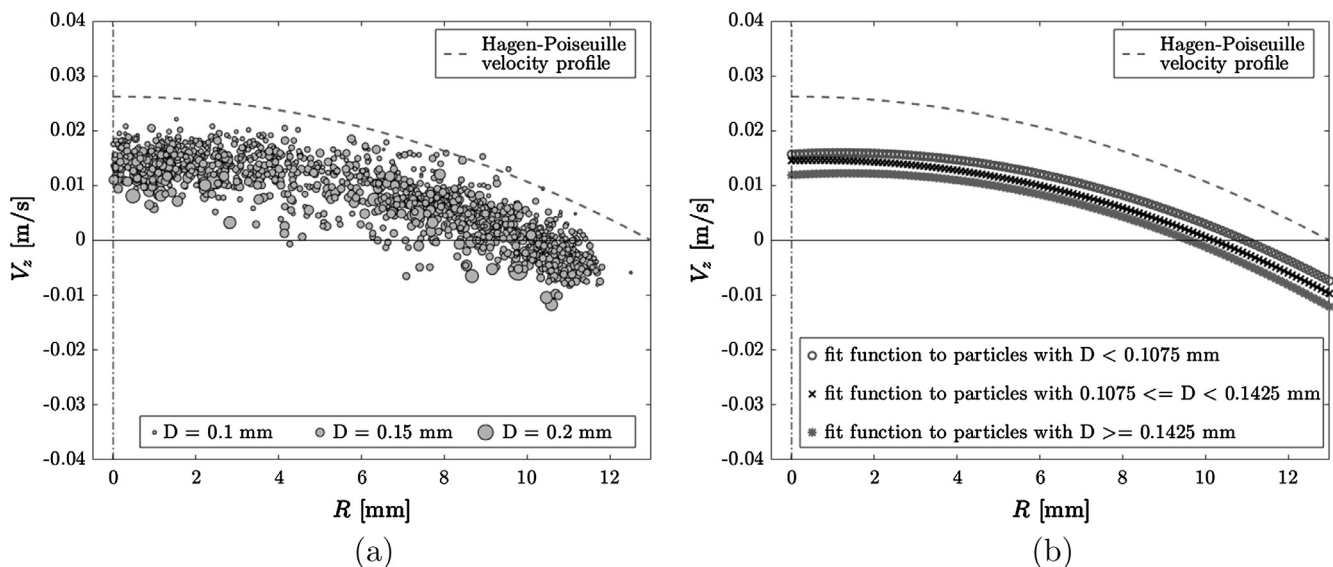



**Fig. 9.** Measured particle vertical velocity, $v_z$, as a function of its radial position in the column, the size of the marker is proportional to its square diameter; (a) - the dashed line represents the analytical solution of the expected Hagen-Poiseuille velocity profile; (b) - The lines represent the quadratic fit curves for particles 95–100 μm (top line), 120–125 μm (middle line), 140—155 μm (bottom line).
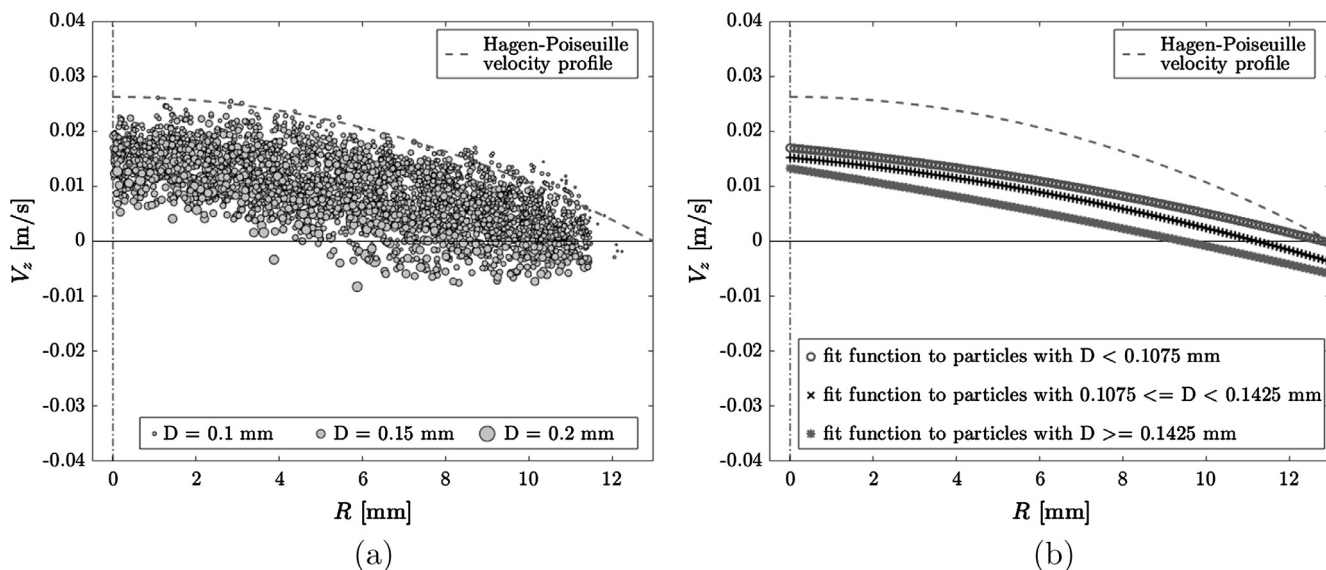
**Fig. 10.** Computed particle vertical velocity, $v_z$, as a function of its radial position in the column; the size of the marker is proportional to its square diameter; (a) - the dashed line represents the analytical solution of the expected Hagen-Poiseuille velocity profile; (b) - the solid lines represent the quadratic fit curves for particles 95–100 μm (top line), 120–125 μm (middle line), 140–155 μm (bottom line).
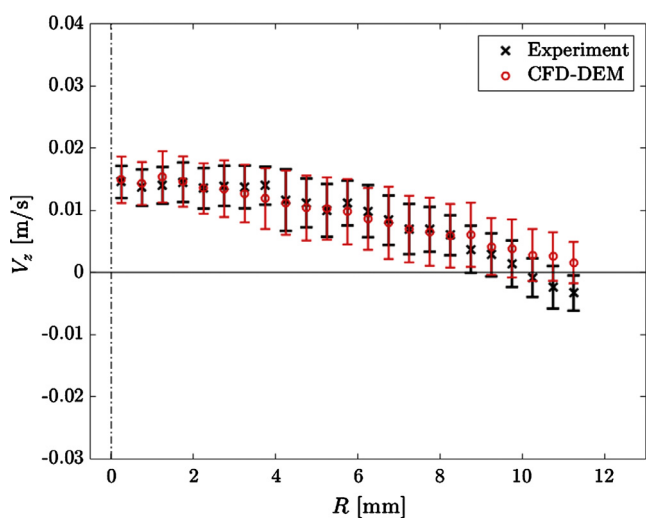


**Fig. 11.** Comparison of the average vertical velocity, $v_z$, of the fluidized glass particles as a function of their radial position in the column (bin size: 0.25 mm) from the experiment (black crosses) and the CFD-DEM simulation (grey circles); error bars indicate the standard deviation around the mean.

inducing recirculation zones behind the nozzles. This leads to a significant change in the fluidized bed height. After identifying this issue, a new sealing system was developed for the outlet nozzles, so that the local flow stays completely undisturbed when the nozzles are closed.

A perfect sealing system would flush the nozzles for the closed case, removing any modification in cross-section. In order to examine this, a simulation was carried out in a geometry with flushed product outlet nozzles (equivalent to a case without product outlet nozzles), which is shown in Fig. 12 (d) and (e). A cause might be the junction to the lower ultrasonic bath, since in the equivalent geometry of Setup 2, the flow is stable laminar (Fig. 12 (f)). Comparing now subfigure (e) to (b), a decrease of the velocity near the wall can be recognized. A further analysis reveals that the flow profile in (e) is close to a parabolic shape and looks more like a laminar profile compared to (b). This first study illustrates how CFD can

help identify and eliminate hydrodynamic problems encountered in the fluidized bed crystallizer. The analysis of such complex hydrodynamic problems is the basis for future geometry optimization.

*4.1.2. Conical part at the bottom of the crystallizer*

Another very critical region in the crystallizer is the nozzle connecting the central crystallizer to the ultrasonic bath through the conical part at the bottom of the crystallizer. It is located very close to the inlet (Fig. 13). At the crystallizer inlet a volume flow rate of 31 L/h is injected into the central crystallizer. At the same time, it is considered that, during normal operation, a volume flow rate of 22 L/h (more than 70% of the injected quantity) escapes the crystallizer toward the ultrasonic bath. Thus, extremely high velocity gradients are found in the lower part of the crystallizer, since large flow quantities travel almost in opposite directions in this region. This is illustrated in Fig. 13 (left), where the magnitude of the velocity field is shown in the bottom part of the crystallizer. A large part of the injected solution might turn and escape the crystallizer immediately toward the ultrasonic bath, without participating into the process (short-cut), which would severely impact process efficiency.

Fig. 13 (left) shows that large-scale vortical structures appear near the nozzle leading to the ultrasonic bath when operating the system as planned. This means that strong flow perturbations are to be expected in the lower part of the central crystallizer, with large unsteady effects. To further investigate this point, it was assumed in a second simulation that the nozzle leading to the ultrasonic bath is now closed, injecting only the difference between both amounts through the central injection: 9 L/h (= 31 L/h–22 L/h). As expected, a stable laminar flow is obtained for these conditions, demonstrating that the nozzle leading to the ultrasonic bath is indeed solely responsible for the observed flow instabilities.

To further quantify the observed difference, the velocity magnitudes along the vertical central axis of the crystallizer are compared in Fig. 14 when opening or closing the nozzle leading to the ultrasonic bath.

Obviously, the two curves differ considerably in the lower, conical part of the crystallizer. With an open ultrasonic bath there are
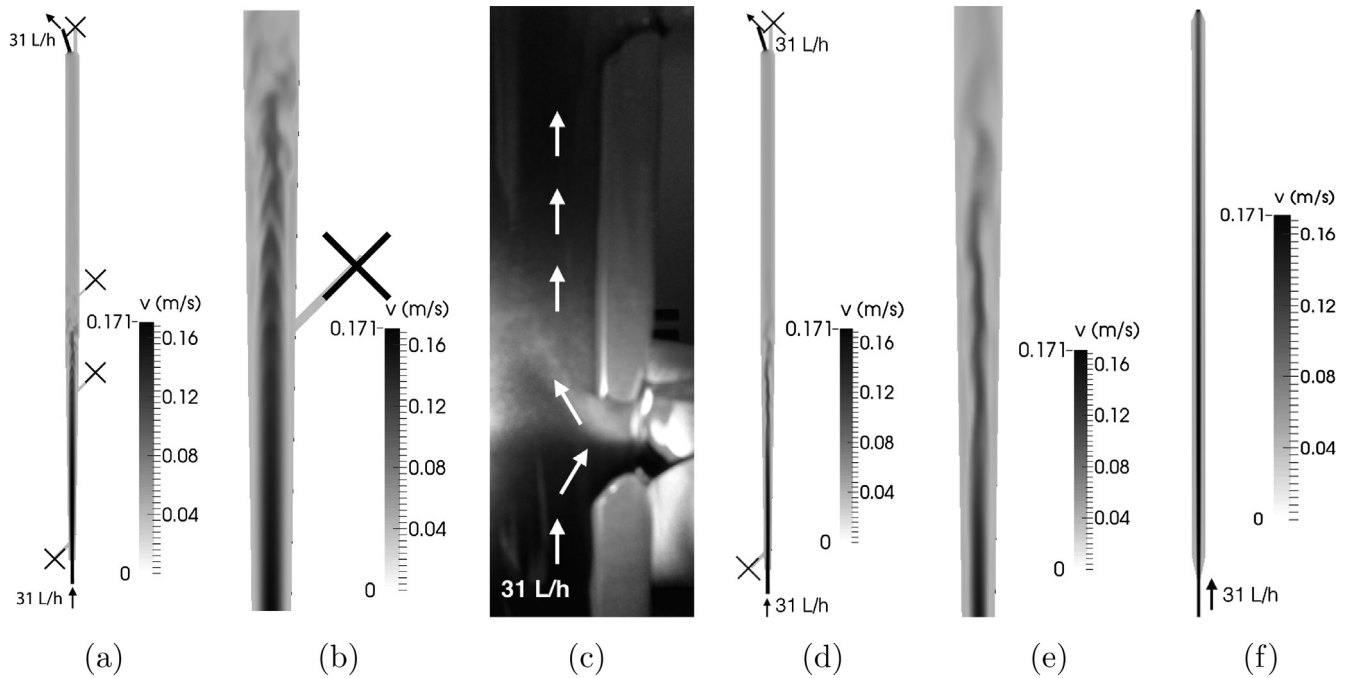
Fig. 12. (a) - Velocity magnitude in the central section plane of the crystallizer (Setup 1) at 180 s, (b) - Close-up view of the velocity field in the crystallizer at mid-height, near the product outlet nozzle, (c) - Close-up view near the product outlet nozzle in the experiment when injecting glass particles as tracers. (d) - Velocity magnitude in the central section plane of the crystallizer with flushed nozzles at 180 s, (e) - Close-up view of the velocity field in the crystallizer with flushed nozzles at mid-height, near the product outlet nozzle, (f) - Velocity magnitude in the central section plane of the test crystallizer (Setup 2) at 180 s.
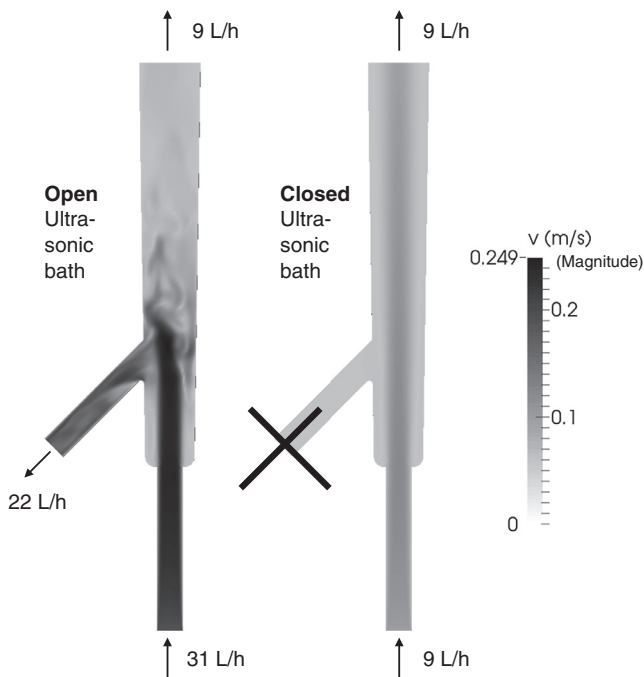


Fig. 13. Instantaneous velocity magnitude at a time of 180 s in the lower, conical part of the crystallizer with the injection tube and nozzle connecting the central crystallizer to the ultrasonic bath. Left: nozzle to ultrasonic bath open. Right: nozzle to ultrasonic bath closed.
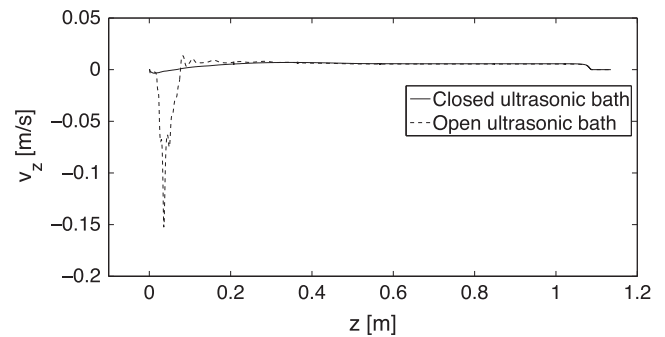


Fig. 14. Instantaneous velocity magnitude along the vertical centerline within the crystallizer (bottom: left; top: right). Dashed line: open ultrasonic bath; Solid line: closed ultrasonic bath.

significantly higher velocity peaks and gradients up to a height of 0.3 m, with much more complex hydrodynamic features, as shown by the oscillating curve. However, in the upper region, the two curves become identical. This demonstrates that, for reduced models (as used for instance in the companion study in Mangold et al.

(2014)) the existence of the ultrasonic bath can be neglected when concentrating the study on the central part of the crystallizer, where product extraction takes place. On the other hand, when trying to improve the flow conditions in the lower part of the crystallizer, simulations must fully take at least the first 0.3 m of the central crystallizer into account. These hydrodynamic investigations are the basis for a currently running geometric optimization of this region. Keeping the geometry of Setup 1 unchanged, the last section of this article investigates the crystallizer with asparagine monohydate crystals in water (neglecting crystal growth).

## 4.2. CFD-DEM simulation of asparagine crystals within the crystallizer

Figs. 15 and 16 depict the vertical relative velocity, $v_z = v_{fluid} - v_{crystal}$, of the fluidized asparagine crystals as a function of their radial position in the crystallizer, with a closed ultrasonic bath or an open ultrasonic bath, respectively. The relative velocity of the crystals is one of the most important physical properties for the
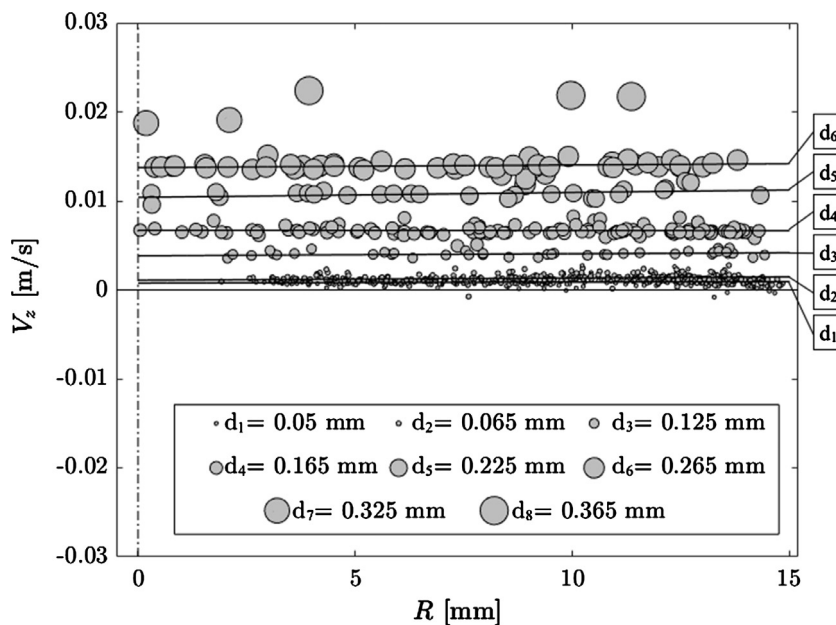
**Fig. 15.** Vertical relative velocity, $v_z$, of fluidized asparagine crystals as a function of their radial position in the crystallizer with a closed ultrasonic bath at the section plane of the product outlet nozzle ($z = 0.525$ m); the size of the marker is proportional to the particle square diameter. The solid lines represent the linear fit curves for particles of 50, 65, 125, 165, 225, and 265 μm (from bottom line to top line, respectively). Since there are very few particles of 325 μm and 365 μm, those are not included in the analysis.
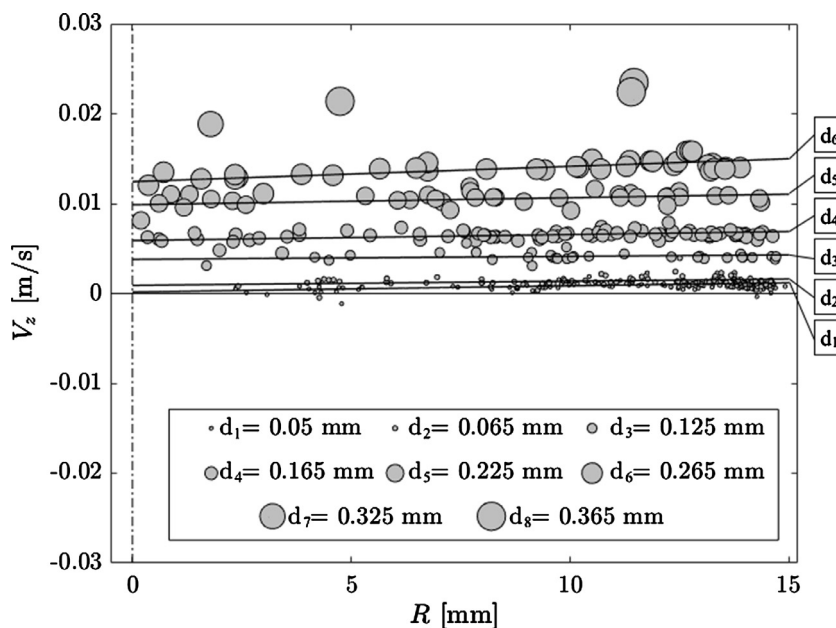


**Fig. 16.** Vertical relative velocity, $v_z$, of fluidized asparagine crystals as a function of their radial position in the crystallizer with an open ultrasonic bath at the section plane of the product outlet nozzle ($z = 0.525$ m); the size of the marker is proportional to the particle square diameter. The solid lines represent the linear fit curves for particles of 50, 65, 125, 165, 225, and 265 μm (from bottom line to top line, respectively). Since there are very few particles of 325 μm and 365 μm, those are not included in the analysis.

process, since crystal growth is influenced directly by it (Ashraf Ali et al., 2013, 2015). The results are shown at mid-height in the column, in the section plane where the product outlet nozzle is mounted ($z = 0.525$ m). The size of each marker is again proportional to the square diameter of the particle. These results are plotted at a physical time of 15 s. An animation showing the motion of all crystals simulated by CFD-DEM in the closed ultrasonic bath is available online as supplementary material to this article.

Confirming Fig. 14, it is observed that the vertical relative velocity, $v_z$, of the crystals at this position is not noticeably impacted by opening or closing the ultrasonic bath. This study confirms that reduced models like those developed, for instance, in Mangold et al. (2014) may safely be used in the central part of the crystallizer, where the target product is extracted.

Most large crystals (above 265 μm) sink downwards and only few large crystals appear at this level after 10 s. In contrast, crystals below this critical size are fluidized and hence show characteristic

vertical relative velocities as a function of crystal diameter: The largest crystals show the highest vertical relative velocity; this relative velocity decreases with decreasing diameter. Thus crystals fractions with identical crystal diameter can be identified by relative velocity, under the condition that the particles are spherical and the fluid velocity is know precisely. The solid lines represent the linear fit curves for particles of 50, 65, 125, 165, 225, and 265 µm (from bottom line to top line, respectively). Since there are very few particles of 325 µm and 365 µm, those are not included in the analysis.

## 5. Conclusion and outlook

In this study a fluidized bed crystallizer was investigated using CFD-DEM simulations and companion validation experiments, focussing on the resulting two-phase flow.

To validate the coupled CFD-DEM model, experiments were first carried out using glass beads with a narrow size distribution. Additionally, compared to the real process, a reduced suspension density was used. Considering 100 000 particles in the simplified setup, comparisons with experimental data demonstrate that CFD-DEM simulations are well suited to predict particle positions and velocities. In particular, the transition point between crystals transported toward the top of the crystallizer (close to the central axis) and crystals sinking down toward the bottom (near the walls) is well reproduced by the simulation.

In order to identify critical hydrodynamic regions in the crystallizer, a single-phase CFD simulation was carried out. This showed that the original extraction nozzles had a negative impact on local hydrodynamics. This problem was solved by a corresponding design modification. Additionally, at the bottom part of the crystallizer, inflow fluxes interact with the outlet to the ultrasonic bath, leading to large flow fluctuations. This observation is used for current design optimization.

Finally, the validated model was used to determine the velocity and position of asparagine crystals within the real crystallizer. These are two essential parameters in controlling process outcome. Corresponding CFD-DEM simulations demonstrate that the setup was designed correctly and, as expected, leads to a fluidization region near the product extraction nozzle, small crystals leaving the draft tube at the top, while large crystals sink down to the ultrasonic bath to be crushed. Additionally, these simulations support model reduction carried out in a companion project (Mangold et al., 2014), since the complex flow features found near the bottom of the crystallizer do not noticeably impact the process outcome above $z \geqslant 0.3$ m. Near the product outlet, reduced models should thus be able to deliver an accurate estimate.

In the full-scale crystallizer, it is currently impossible to consider the real suspension density. A possible solution could be found in systematic similarity theory, as already used in a number of publications (e.g., Heinrich et al., 2015; Sutkar et al., 2013; Link et al., 2009; Sakai and Koshizuka, 2009; Jajcevic et al., 2013, in which the particle number is decreased while simultaneously increasing the particle diameter. However, these publications have shown that the ratio between artificial and real particle diameter should be less than 3 for accurate results. In the crystallizer considered for this study, a ratio of at least 12 would be necessary, with an additional reduction in crystallizer size. Therefore, an improved coarse-graining approach will be necessary for the considered application, involving solid–liquid systems. Future studies will show whether this approach might surpass the current combination of model reduction (Mangold et al., 2014) and short-time full-scale CFD-DEM studies at reduced particle density for the planned process optimization. Simulations involving repeated, short-time CFD-DEM simulations combined with in-between 0D computations of crystal growth based on the relative velocities obtained are currently being started.

## Appendix A. Supplementary material

Supplementary data associated with this article can be found, in the online version, at http://dx.doi.org/10.1016/j.ces.2017.01.068.

## References

Ashraf Ali, B., Janiga, G., Temmel, E., Seidel-Morgenstern, A., Thévenin, D., 2013. Numerical analysis of flow characteristics and crystal motion in a batch crystallizer. J. Cryst. Growth 372, 219–229.
Ashraf Ali, B., Börner, M., Peglow, M., Janiga, G., Seidel-Morgenstern, A., Thévenin, D., 2015. Coupled computational fluid dynamics-discrete element method simulations of a pilot-scale batch crystallizer. Crystal Growth Des. 15, 145–155.
Binev, D., 2015. Continuous fluidized bed crystallization PhD Thesis. University of Magdeburg "Otto von Guericke".
Binev, D., Seidel-Morgenstern, A., Lorenz, H., 2016. Continuous separation of isomeres in fluidized bed crystallizers. Crystal Growth Des. 16, 1409–1419.
Blais, B., Lassaigne, M., Goniva, C., Fradette, L., Bertranda, F., 2016. Development of an unresolved CFD-DEM model for the flow of viscous suspensions and its application to solid-liquid mixing. J. Comput. Phys. 318, 201–221.
Chen, Y., Lim, C.J., Grace, J.R., Zhang, J., Zhao, Y., Zheng, C., 2015. Characterization of pressure fluctuations from a gas-solid fluidized bed by structure density function analysis. Chem. Eng. J. 129, 156–167.
Crowe, C.T., 2005. Multiphase Flow Handbook. Taylor and Francis, Boca Raton, USA. ISBN: 9780849312809.
Cundall, P.A., Strack, O.D.L., 1979. A discrete numerical model for granular assemblies. Géotechnique 29 (1), 47–65.
Daróczy, L., Janiga, G., Thévenin, D., 2014. Systematic analysis of the heat exchanger arrangement problem using multi-objective genetic optimization. Energy 65, 364–373.
Di Felice, R., 1993. The voidage function for fluid-particle interaction systems. Int. J. Multiph. Flow 20 (1), 153–159.
Eicke, M., Levilain, G., Seidel-Morgenstern, A., 2013. Efficient resolution of enantiomers by coupling preferential crystallization and dissolution. Crystal Growth Des. 13, 1638–1648.
Fang, C., Lu, X., Buijs, W., Fan, Z., Güner, F.E.G., van Huis, M.A., Witkamp, G.-J., Vlugt, T.J.H., 2015. Crystal structure, stability, and electronic properties of hydrated metal sulfates MSO4(H2O)n (M = Ni, Mg; n=6, 7) and their mixed phases: a first principles study. Chem. Eng. Sci. 121, 77–86.
Fayzullin, R., Lorenz, H., Bredikhina, Z., Bredikhin, A., Seidel-Morgenstern, A., 2014. Solubility and some crystallization properties of conglomerate forming chiral drug guaifenesin in water. J. Pharm. Sci. 10, 3176–3182.
Freireich, B., Litster, J., Wassgren, C., 2015. Using the discrete element method to predict collision-scale behavior: a sensitivity analysis. Chem. Eng. Sci. 274, 3407–3416.
Fries, L., Antonyuk, S., Heinrich, S., Palzer, S., 2011. DEM-CFD modeling of a fluidized bed spray granulator. Chem. Eng. Sci. 66, 2340–2355.
Fries, L., Antonyuk, S., Heinrich, S., Dopfer, D., Palzer, S., 2013. Collision dynamics in fluidised bed granulators: a DEM-CFD study. Chem. Eng. Sci. 98, 298–310.
C. Goniva, C. Kloss, CFDEMcoupling Documentation, www.cfdem.com (accessed July 5, 2016).
C. Goniva, C. Kloss, CFDEM Project, www.cfdem.com (accessed July 5, 2016).
Goniva, C., Kloss, C., Hager, A., Pirkers, S., 2010. An open source CFD-DEM perspective. In: Proceedings of 5th OpenFOAM workshop Gothenburg, Sweden, June 21–24.
Goniva, C., Kloss, C., Deen, N.G., Kuipers, J.A.M., Pirkers, S., 2012. Influence of rolling friction on single spout fluidized bed simulation. Particuology 10, 582–591.
Harris, C.K., Roekaerts, D., Rosendal, F.J.J., Buitendijk, F.G.J., Daskopoulos, P., Vreenegoor, A.J.N., Wang, H., 1996. Computational fluid dynamics for chemical reactor engineering. Chem. Eng. Sci. 51, 1569–1594.
Heinrich, S., Dosta, M., Antonyuk, S., 2015. Multiscale analysis of a coating process in a Wurster fluidized bed apparatus. Adv. Chem. Eng. 46, 83–135.
Hertz, H., 1882. Über die Berührung fester elastischer Körper (in German). J. Reine Angew. Math. 92, 156–171.
Jajcevic, D., Siegmann, E., Radeke, C., Khinast, J.G., 2013. Large-scale CFD-DEM simulations of fluidized granular systems. Chem. Eng. Sci. 98, 298–310.
Link, J.M., Godlieb, W., Tripp, P., Deena, N., Heinrich, S., Kuipers, J., Schönherr, M., Peglow, M., 2009. Comparison of fibre optical measurements and discrete

element simulations for the study of granulation in a spout fluidised bed. Powder Technol. 189, 202–217.

Lorenz, H., Seidel-Morgenstern, A., 2014. Processes to separate enantiomers. Angew. Chem. Int. Ed. 53, 1218–1251.

Mangold, M., Khlopov, D., Danker, G., Palis, S., Svjatnyj, V., Kienle, A., 2014. Development and nonlinear analysis of dynamic plant models in ProMoT/Diana. Chem. Ing. Tech. 86, 1107–1116.

Mindlin, R., 1949. Compliance of elastic bodies in contact. J. Appl. Mech. 16, 259–268.

Müller, P., Tomas, J., 2014. Simulation and calibration of granules using the discrete element method. Particuology 12, 40–43.

Ochsenbein, D.R., Schorsch, S., Salvatori, F., Vetter, T., Morari, M., Mazzotti, M., 2015. Modeling the facet growth rate dispersion of $\beta$-glutamic acid – combining single crystal experiments with nD particle size distribution data. Chem. Eng. Sci. 133, 30–43.

Qamar, S., Galan, K., Elsner, M.-P., Hussain, I., Seidel-Morgenstern, A., 2013. Theoretical investigation of simultaneous continuous preferential crystallization in a coupled mode. Chem. Eng. Sci. 98, 25–39.

Qiu, L., Wu, C., 2014. A hybrid DEM/CFD approach for solid-liquid flows. J. Hydrodynam. 26, 19–25.

Reinhold, A., Briesen, H., 2015. High dimensional population balances for the growth of faceted crystals: combining Monte Carlo integral estimates and the method of characteristics. Chem. Eng. Sci. 127, 220–229.

Sakai, M., Koshizuka, S., 2009. Large-scale discrete element modeling in pneumatic conveying. Chem. Eng. Sci. 64, 533–539.

Salikov, V., Antonyuk, S., Heinrich, S., Sutkar, V., Deen, N., Kuipers, J., 2015. Characterization and CFD-DEM modelling of a prismatic spouted bed. Powder Technol. 270, 622–636.

Sommerfeld, M., van Wachem, B., Oliemans, R., 2008. Best practice guidelines for computational fluid dynamics of dispersed multi-phase flows. ERCOFTAC. ISBN: 978-91-633-3564-8.

Sutkar, V.S., Deen, N.G., Mohan, B., Salikov, V., Antonyuk, S., Heinrich, S., Kuipers, J., 2013. Numerical investigations of a pseudo-2D spout fluidized bed with draft plates using a scaled discrete particle model. Chem. Eng. Sci. 104, 790–807.

The OpenFOAM Foundation, Openfoam 2.2.x, www.openfoam.org (accessed July 5, 2016).

Verein deutscher Ingenieure (VDI-GVC), VDI - Wärmeatlas. Recherchieren - Berechnen - Konstruieren, Springer Verlag, 8. Auflage, Berlin, Heidelberg, 1997.

Wu, C.L., Ayenia, O., Berrouk, A.S., Nandakumara, K., 2014. Parallel algorithms for CFD-DEM modeling of dense particulate flows. Chem. Eng. Sci. 118, 221–244.

Zhou, Z.Y., Pinson, D., Zou, R.P., Yu, A.B., 2011. CFD-DEM simulation of gas fluidization of ellipsoidal particles. Chem. Eng. Sci. 66, 6128–6145.

Zhu, H.P., Zhou, Z.Y., Yang, R.Y., Yu, A.B., 2007. Discrete particle simulation of particulate systems: theoretical developments. Chem. Eng. Sci. 62, 3378–3396.

Zhu, H.P., Zhou, Z.Y., Yang, R.Y., Yu, A.B., 2008. Discrete particle simulation of particulate systems: a review of major applications and findings. Chem. Eng. Sci. 63, 5728–5770.